

Macroscopic entanglement between localized domain walls inside a cavity

Rahul Gupta,^{1,*} Huaiyang Yuan,² and Himadri Shekhar Dhar^{1,3}

¹*Department of Physics, Indian Institute of Technology Bombay, Powai, Mumbai 400076, India*

²*Institute for Advanced Study in Physics, Zhejiang University, 310027 Hangzhou, China*

³*Centre of Excellence in Quantum Information, Computation, Science and Technology,
Indian Institute of Technology Bombay, Mumbai 400076, India*

(Dated: August 6, 2025)

We present a scheme for generating stable and tunable entanglement between two localized Bloch domain walls in nanomagnetic strips kept inside a chiral optical cavity. The entanglement is mediated by the effective optomechanical interaction between the cavity photons and the two macroscopic, collective modes of the pinned domain walls. By controlling the pinning potential and optical driving frequency, the robust, steady-state entanglement between the two macroscopic domain walls can survive beyond the typical milli-Kelvin temperature range.

I. INTRODUCTION

The field of quantum magnonics [1, 2] has seen rapid growth, driven by the quest to harness the coherent properties of quantized collective spin waves in magnetic materials or magnons for emerging quantum technologies and solid-state device applications. For instance, hybrid quantum systems [3–5] that combine magnons with other quantum systems such as photonic cavities or superconducting circuits provide a platform to perform a variety of quantum operations [6], ranging from quantum computing [7] and storage [8] to quantum transduction [9].

While much of the current focus in quantum magnonics has been on propagating magnons [10], localized magnetic spin textures such as chiral domain walls [11, 12], skyrmions [13], and spin vortices [14] can offer additional advantages for quantum computing and related applications. These textures can be spatially pinned [15–17] and arranged [18], readily observed [19, 20], and also transported in magnetic racetrack circuits [21]. Furthermore, they often exhibit rich topological properties [22, 23], making them attractive for both classical [24–26] and quantum [27, 28] information processing.

An essential task in implementing key quantum protocols is to generate and control entanglement, which has been extensively explored in propagating magnon modes [29–34]. Most of these schemes rely on strong nonlinearity to generate entanglement either using Kerr effect [30], squeezed light [32] or optomechanical coupling in nonstationary magnon states [31]. However, generating stable, steady-state entanglement in localized spin textures remains largely unexplored. Recent experimental progress has significantly improved the ability to manipulate spin textures such as a Bloch domain wall (DW), especially in uniaxial magnetic materials [35]. These spin textures are already widely used in classical spintronic and nanoelectronic applications [36, 37] and can operate at much lower energies compared to their electronic counterparts. Importantly, in the quantum regime these DW

behave as a macroscopic quasiparticle [38], and extending their control into the quantum domain, especially by inducing entanglement and squeezing simply through external driving, opens up exciting new opportunities for quantum information processing, computing, and memory applications.

In this work, we propose a compelling scheme to resolve the outstanding problem of entanglement in localized spin textures, by generating highly tunable and robust macroscopic entanglement between pinned Bloch domain walls in magnetic strips placed inside a chiral optical cavity [39]. The photons inside the cavity create a radiation pressure on the two DWs through the inverse Faraday effect and generate an effective optomechanical interaction between the cavity mode and the macroscopic DW modes [38]. To achieve stable entanglement, we exploit the theoretical machinations of cavity optomechanics [40] to explore the dissipative phases of the system and identify phases with stable steady-state solutions, by tuning the pinning potential and the optical driving frequency. We observe that the domain walls are strongly entangled to the photonic mode close to the transition boundaries between two stable dissipative phases. The entanglement is robust across a broad range of optical power and can be controlled by the external field. For example, when DW frequencies are different, the driving can be varied to entangle either one of the domain walls with the photonic mode. On the other hand, for identical DW frequencies, we can use the driving to continuously reduce the entanglement between the domain wall and photon modes in lieu of building strong entanglement between the two macroscopic, Bloch domain walls. Remarkably, the entanglement here is generated and controlled through the driven-dissipative properties of an optomechanical system rather than by introducing strong external nonlinearities in the dynamics.

The paper is arranged in the following way. In Sec. II, the setup and theoretical model for the interaction of DWs with a cavity field is proposed. Section III discusses distinct dissipative phases and their entanglement properties. This is followed by Sec. IV, where the origin of macroscopic DW entanglement and its thermal sta-

* rahul.quantumfield@iitb.ac.in

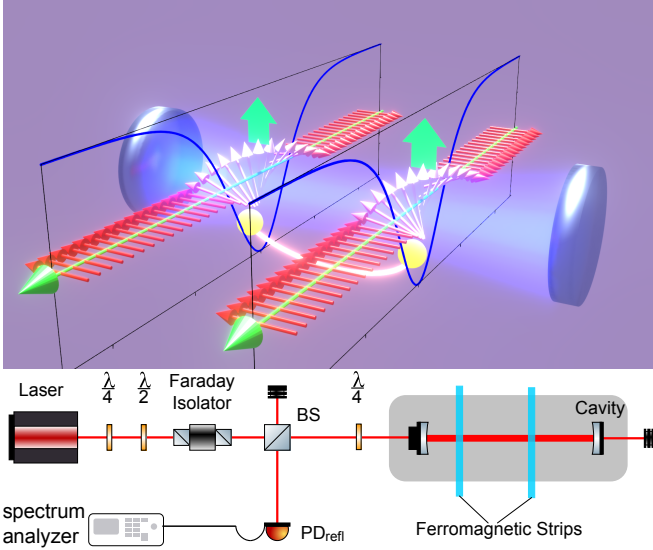


FIG. 1. Experimental setup. The illustration shows a linearly polarized light created by controlling waveplates, which is passed through a Faraday isolator and quarter wave plate to excite circularly polarized optical mode. This creates a standing wave inside the cavity which is coupled to two ferromagnetic strips. The Bloch walls in the strips are pinned where the cavity field is present. The reflected optical mode is then collected at photodiode (PD) and analyzed via a spectrum analyzer. The output and input are separated using a beams-splitter (BS) and waveplate arrangement.

bility are presented. We conclude with a discussion and outlook in Sec. V.

II. SETUP AND THEORETICAL MODEL

The primary objective of our work is to generate stable entanglement between two localized Bloch domain walls in spatially separated magnetic strips placed inside a single mode, chiral cavity. As such the setup of our protocol involves two key components viz., the domain wall and the chiral cavity.

Magnetic spin textures such as a domain wall (DW) occur naturally in a range of magnetic materials [41–43] and have rich topological structure that depend on the bulk properties and can majorly be classified in two types: Bloch walls and Neel walls [44]. These DWs can be localized spatially or pinned using various mechanisms [45–48]. Secondly, chiral cavities [49] are designed to excite a single polarization state such as left or right circularly polarized light. Such single-handed cavities have recently been demonstrated [39] and used for generating strong coupling with chiral molecules [50]. An illustration of the setup involving Bloch DWs in ferromagnetic strips inside an optical cavity is shown in Fig. 1. The magnetic strips are placed in such a way that the polarized light inside the cavity passes through the center of the pinned Bloch DWs. The radiation pressure forces the

pinned magnon modes of the DW to oscillate due to the inverse Faraday effect. For a strong pinning potential, the magnon mode behaves like a collective macroscopic particle and can be canonically quantized to resemble a quantum harmonic oscillator [38].

Under this quantized picture, the Hamiltonian of the system, neglecting the dissipation effects, can be written as $\mathcal{H} = \mathcal{H}_0 + \mathcal{H}_{\text{int}} + \mathcal{H}_L$, where the terms represent the non-interacting, interacting and the driving, respectively. For N ferromagnetic strips inside a single-mode chiral cavity, with frequencies ω_j and ω_a , respectively, the non-interacting Hamiltonian is given by ($\hbar = 1$),

$$\mathcal{H}_0 = \omega_a a^\dagger a + \sum_{j=1}^N \omega_j b_j^\dagger b_j, \quad (1)$$

where a and b_1, b_2, \dots, b_N are the bosonic operators for the cavity and the N magnon modes. Each DW is pinned to a frequency $\omega_j = \sqrt{2K_{\text{pin}}^j K_\perp l / \hbar^2 \lambda_{\text{DW}}}$ that can be individually controlled by varying the pinning field. Here, K_{pin}^j is the anisotropic pinning field strength, K_\perp is the out of plane anisotropy parameter of the magnetic insulator with unit cell dimension l , and λ_{DW} is the effective DW length. The interaction [38, 40] and driving Hamiltonian $\mathcal{H}_1 = \mathcal{H}_{\text{int}} + \mathcal{H}_L$ is given by

$$\mathcal{H}_1 = \sum_{j=1}^N g_j a^\dagger a (b_j^\dagger + b_j) + i(a^\dagger \xi e^{-i\omega_L t} - a \xi^* e^{i\omega_L t}), \quad (2)$$

where g_j is the coupling between a photon and the j^{th} magnon mode arising due to inverse Faraday effect and ξ is the strength of the driving field with frequency ω_L . The magneto-optic coupling term is given by $g_j = -c\phi_F \sqrt{\epsilon} S_{\text{eff}}^j / 2$, and creates an effective optomechanical interaction between the cavity and magnon modes. This is independent of the cavity frequency ω_a , unlike the usual optomechanical coupling where $g_j \propto \omega_a$ [40], and is dependent on the Faraday rotation ϕ_F , which is the amount of rotation in polarization per unit length as light passes through a material of dielectric permittivity ϵ . S_{eff}^j is a dimensionless geometrical factor that depends on the scattering cross-section, cavity volume and zero point fluctuation. See Appendix A for more details. The higher-order terms and non-linear Kerr effect have been neglected. In the frame moving with the driving field i.e., under the unitary transformation $\mathcal{H}' = \mathcal{U} \mathcal{H} \mathcal{U}^\dagger - i\hbar \mathcal{U} \frac{\partial \mathcal{U}^\dagger}{\partial t}$, where $\mathcal{U} = e^{i\omega_L a^\dagger a t}$, the Hamiltonian is time-independent

$$\begin{aligned} \mathcal{H}' = & -\Delta_a a^\dagger a + \sum_{j=1}^N \left[\omega_j b_j^\dagger b_j + g_j (b_j^\dagger + b_j) a^\dagger a \right] \\ & + i\xi (a^\dagger - a), \end{aligned} \quad (3)$$

where $\Delta_a = \omega_L - \omega_a$, is the cavity detuning.

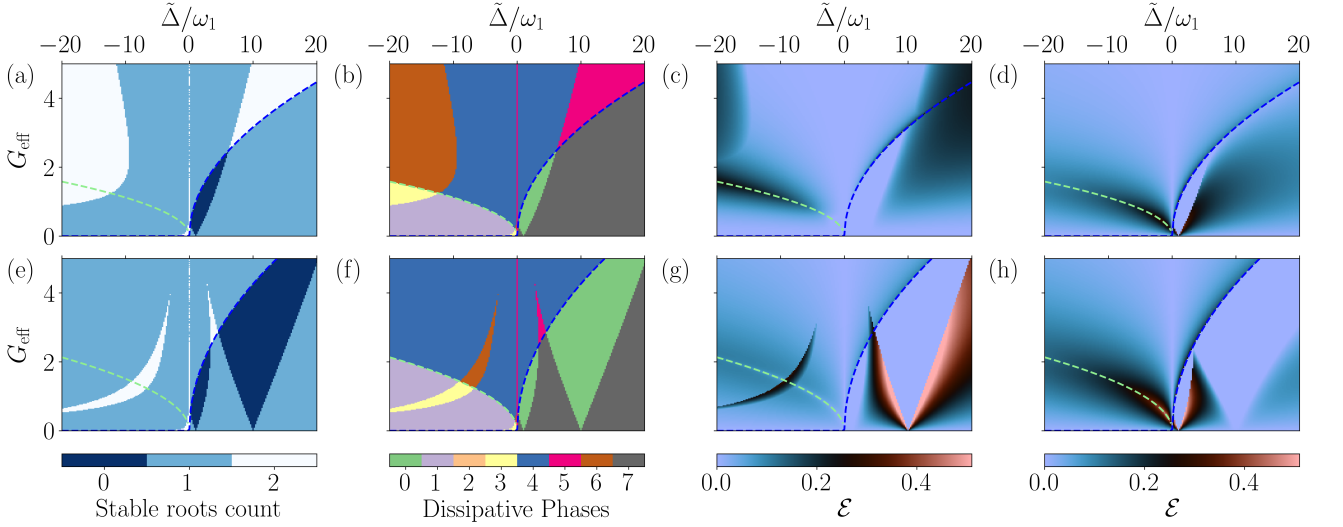


FIG. 2. Dissipative phases and two-mode entanglement of the system as a function of the detuning $\tilde{\Delta}$ and $G_{\text{eff}} = G|g_1|/\omega_1$ for $\omega_2 = \omega_1$ (top row) and $\omega_2 = 10 \omega_1$ (bottom row). The plots (a) and (e) show the number of stable solutions, with the distinct dissipative phases shown in (b) and (f). The entanglement between the two DWs $\mathcal{E}_{1|2}$ and between the photon and DW modes $\mathcal{E}_{a|1(2)}$ are shown in plots (c) and (g). Finally, the plots (d) and (h) show the entanglement between the photon and DW modes $\mathcal{E}_{a|1}$ and $\mathcal{E}_{a|2}$ for $\omega_2 = 10 \omega_1$. The blue and green dashed lines highlight two interesting regions of phase transition. The former indicates the jump from a region with two to three real solutions, while the latter exhibits a line of transcritical bifurcation where $\mathcal{E}_{1|2}$ in plot (c) is optimal. The parameters taken are $\kappa_a = 2$ MHz, $\kappa_{1(2)} = 1$ MHz, $\omega_1 = 1$ GHz, $g_{1(2)} = 1$ MHz and temperature $T = 2$ mK.

III. STABLE ENTANGLED PHASES

Since our goal is to generate stable steady-state entanglement, it is important to first identify the driven dissipative phases of the system with stable solutions [51]. To this effect, the Hamiltonian in Eq. (3) is linearized around the steady state photon number \bar{n}_a . In the limit of strong driving, \bar{n}_a is obtained as the roots of the cubic equation $\bar{n}_a = |\xi|^2 / [(\Delta_a + \Omega \bar{n}_a)^2 + \kappa_a^2]$, where $\Omega = \sum_{j=1}^2 2g_j^2 \omega_j / (\omega_j^2 + \kappa_j^2)$, and κ_a and κ_j are the dissipation rates in cavity and j^{th} DW mode, respectively. The steady states of the different operators are written as $\langle a \rangle = \alpha^{(k)}$, $\langle a^\dagger a \rangle = \bar{n}_a^{(k)}$, and $\langle b_j \rangle = \beta_j^{(k)}$, where $k \in \{0, 1, 2\}$ indicate the roots (see Appendix B for the derivation). Let $G^2 \equiv \bar{n}_a^{(k=0)}$ denote the real root common to all parameter regimes, with $G = |\xi| / \sqrt{\tilde{\Delta}^2 + \kappa_a^2}$, where $\tilde{\Delta} = \Delta_a + \Omega G^2$. The advantage of this representation is that $\bar{n}_a^{(k)}$ corresponding to the other roots can be parametrized in terms of G and $\tilde{\Delta}$, such that for $k \in \{1, 2\}$

$$\bar{n}_a^{(k)} = \frac{G^2}{2} - \frac{\tilde{\Delta}}{\Omega} + (-1)^{k-1} \sqrt{\left(\frac{G^2}{2} - \frac{\tilde{\Delta}}{\Omega}\right)^2 - \frac{\kappa_a^2 + \tilde{\Delta}^2}{\Omega^2}}. \quad (4)$$

Since complex roots appear in conjugates, the system can have either one or three real roots. For the latter, the parameters must satisfy the positive discriminant condition

in Eq. (4), $G^2 \geq 2\Omega^{-1}(\tilde{\Delta} + \sqrt{\kappa_a^2 + \tilde{\Delta}^2})$. The blue-dashed line separating the two regimes is shown in Fig. 2.

Let us now focus on the case of two ferromagnetic strips ($N = 2$) inside the cavity. The DW in each strip is pinned with different potentials leading to two magnon modes with frequencies ω_1 and ω_2 . The effective Hamiltonian linearized around $\bar{n}_a^{(k)}$ is given by

$$H_{\text{eff}} = -\tilde{\Delta}^{(k)} a^\dagger a + \omega_1 b_1^\dagger b_1 + \omega_2 b_2^\dagger b_2 + \left(\alpha^{(k)} a^\dagger + \alpha^{(k)*} a \right) \times \left[g_1(b_1 + b_1^\dagger) + g_2(b_2 + b_2^\dagger) \right], \quad (5)$$

where $\tilde{\Delta}^{(k)} = \Delta_a - 2\text{Re}(\beta_j^{(k)})$. To analyze the stability of the dissipative phases, we study the linearized quantum Langevin equations (QLE) [40] for $u = \{x_i, y_i\}$ for $i \in \{a, 1, 2\}$, where $x_i = (\mathcal{O}_i + \mathcal{O}_i^\dagger)/\sqrt{2}$ and $y_i = i(\mathcal{O}_i - \mathcal{O}_i^\dagger)/\sqrt{2}$ are the quadrature operators for $\mathcal{O}_i \in [a, b_1, b_2]$. For the k^{th} root, the QLE is given by $\dot{u}^{(k)} = A^{(k)} u^{(k)} + \eta$, where $\eta = [\sqrt{2\kappa_i} x_i^{\text{in}}, \sqrt{2\kappa_i} y_i^{\text{in}}]$ and

$$A^{(k)} = \begin{pmatrix} -\kappa_a & -\tilde{\Delta}^{(k)} & -\tilde{g}_1 y_\alpha^{(k)} & 0 & -\tilde{g}_2 y_\alpha^{(k)} & 0 \\ \tilde{\Delta}^{(k)} & -\kappa_a & \tilde{g}_1 x_\alpha^{(k)} & 0 & \tilde{g}_2 x_\alpha^{(k)} & 0 \\ 0 & 0 & -\kappa_1 & \omega_1 & 0 & 0 \\ \tilde{g}_1 x_\alpha^{(k)} & \tilde{g}_1 y_\alpha^{(k)} & -\omega_1 & -\kappa_1 & 0 & 0 \\ 0 & 0 & 0 & 0 & -\kappa_2 & \omega_2 \\ \tilde{g}_2 x_\alpha^{(k)} & \tilde{g}_2 y_\alpha^{(k)} & 0 & 0 & -\omega_2 & -\kappa_2 \end{pmatrix}, \quad (6)$$

where $x(y)_\alpha^{(k)} = \langle x(y)_a^{(k)} \rangle$ and $\tilde{g}_{1(2)} = g_{1(2)}\sqrt{2}$. The stable phases of the system are related to the conver-

gence of the system to a steady state, which requires that $\max\{\text{Re}(\{\lambda_A\})\} \leq 0$, where $\{\lambda_A\}$ are the eigenvalues of the matrix $A^{(k)}$.

In the strong driving regime ($\bar{n}_a \gg 1$), the system is Gaussian and the entanglement between the three modes a, b_1 and b_2 can be quantified by the properties of the steady state covariance matrix $V^{(k)}$ of the system. This can be obtained by solving the Lyapunov equation

$$A^{(k)}V^{(k)} + V^{(k)}A^{(k)T} = -D, \quad (7)$$

where $D = [\{\kappa_i(2n_i^{\text{th}} + 1), \kappa_i(2n_i^{\text{th}} + 1)\}]$ and $n_i^{\text{th}} = 1/(e^{\hbar\omega_i/k_B T} - 1)$ for $i \in \{a, 1, 2\}$. To quantify entanglement between any two of the modes (say the two DW modes), corresponding to the stable root k , we eliminate the third mode (the photon mode) from the covariance matrix. The reduced 4×4 covariance matrix for the two DW modes $\tilde{V}_{12}^{(k)}$ is then used to study entanglement. The measure used is logarithmic negativity (LN), an entanglement monotone based on Simon's criterion [52], given by $\mathcal{E}_{1|2} = \max\{0, \ln(2\mu_-)\}$, where μ_- is the lowest eigenvalue of the symplectically transformed reduced covariance matrix. Similarly, the entanglement $\mathcal{E}_{a|j}$ between the photon and DW mode j is obtained by estimating LN for the reduced covariance matrix $\tilde{V}_{aj}^{(k)}$.

Figure 2 illustrates the stable phases of the driven-dissipative system and the entanglement between the different modes, respectively. These phases are for different values of effective coupling $G_{\text{eff}} = G|g_1|/\omega_1$ and the detuning $\tilde{\Delta}$, which can be controlled by the driving field strength and frequency. Moreover, we consider the cases where the two DW magnon modes are either resonant ($\omega_2 = \omega_1$) or considerably detuned ($\omega_2 = 10\omega_1$), depending on the choice of the pinning field strength at the magnetic strips. The number of stable phases and the different dissipative phases are shown in Figs. 2(a,e) and (b,f), respectively, while Figs. 2(c) and (d,g,h) shows the DW-DW and photon-DW entanglement in the different phases of the system, maximized over all stable roots. Now, the key objective of the work is to demonstrate significant entanglement between the two DW magnon modes. In this regard, it is worth exploring regions where transcritical bifurcation occurs i.e., point where two of the roots exchange their stability (the stable root becomes unstable, while unstable root becomes stable), thus keeping the total number of stable roots fixed and marking a continuous dissipative phase transition. Let us consider the case $\bar{n}_a^{(0)} = \bar{n}_a^{(k)}$ for $k \in \{1, 2\}$, where such a transition occurs at $G = \sqrt{-(\kappa_a^2 + \tilde{\Delta}^2)/2\tilde{\Delta}\Omega}$ for $\tilde{\Delta} \leq 0$. These bifurcations are highlighted in Fig. 2 by a green dashed line. The entanglement properties of the system along this line are remarkable. For $\omega_1 = \omega_2$, the entanglement between photonic modes and the domain wall, $\mathcal{E}_{a|j}$ for $j \in \{1, 2\}$, is maximum close to $\tilde{\Delta} = -\omega_1$, as shown in Figs. 2(c,d). Note that the photon mode is equally entangled with both the DW modes. However, moving away to the left along the transition line

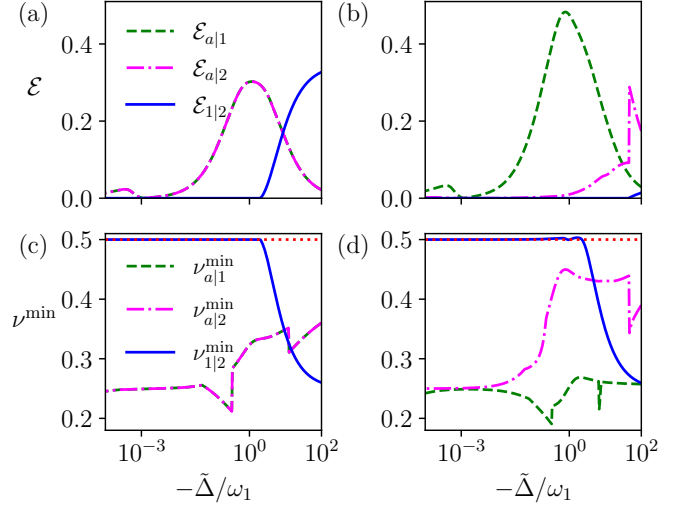


FIG. 3. Entanglement switching and two-mode squeezing. The figure shows (top) bipartite entanglement $\mathcal{E}_{i|j}$ and (bottom) lowest eigenvalue $\nu_{i|j}^{\min}$ of the covariance matrix $\tilde{V}_{i|j}^{(k)}$, between modes i and j (where $i, j \in \{a, 1, 2\}$). The plots are for $\omega_1 = \omega_2$ (a,c) and $\omega_2 = 10\omega_1$ (b,d). All other parameters are same as in Fig. 2.

($\tilde{\Delta} < 0$), the photon-DW entanglement decreases and entanglement between the two DW modes $\mathcal{E}_{1|2}$ becomes significantly stronger. This transition from photon-DW to entanglement between the two magnetic textures is captured in Fig. 3(a). Incidentally, for unequal pinning strengths $\omega_2 = 10\omega_1$, the entanglement between the two DWs is suppressed. Moreover, the photon mode entangles with only one of the DW modes. For instance in Fig. 3(b), the photon mode entangles with the first DW mode at $\tilde{\Delta} = -\omega_1$ i.e., $\mathcal{E}_{a|1}$ is finite. Again by moving along the bifurcation line towards $\tilde{\Delta} = -\omega_2$, the entanglement can switch to the second DW mode and $\mathcal{E}_{a|2}$ is now significant. As such, by controlling the pinning strengths and the detuning, entanglement can be generated between the two DW modes or between the photon and a specific DW mode. Note that the tradeoff of entanglement is enforced by the monogamy principle [53, 54], which restricts the presence of significant entanglement simultaneously between all possible pairs of modes.

IV. MACROSCOPIC ENTANGLEMENT

While entanglement between the photonic and DW modes arise from the direct light-matter coupling in the linearized Hamiltonian in Eq. (5), the generation of entanglement between the two macroscopic DW modes in the absence of any nonlinearity is not straightforward. In our work, this is achieved by using strong coupling to move to an dispersive regime in terms of the effective detuning $\tilde{\Delta}$ from the cavity modes. Mathematically this entails that $\tilde{\Delta} \gg \omega_1, \kappa_a$. In this limit, we adiabatically

eliminate the cavity mode using the steady-state value of the k^{th} root and the relation with the DW mode fluctuations $a = i\alpha \sum_j g_j (b_j + b_j^\dagger) / (i\tilde{\Delta}^{(k)} - \kappa_a)$. The resulting Hamiltonian (derived in Appendix C) is given by

$$H_{ad} = \sum_j \omega_j^{\text{eff}} b_j^\dagger b_j + \sum_{i,j}^{j \neq i} G_{ij}^{\text{eff}} (b_i + b_i^\dagger) (b_j + b_j^\dagger), \quad (8)$$

where, the effective mode frequency is $\omega_j^{\text{eff}} = \omega_j + G_{jj}^{\text{eff}}$, with $G_{ij}^{\text{eff}} = \tilde{\Delta}^{(k)} |\alpha|^2 g_i g_j / (\tilde{\Delta}^{(k)2} + \kappa_a^2)$.

The coupling between the two DW modes b_i and b_j are governed by G_{ij}^{eff} , which increases with the effective detuning $\tilde{\Delta}^{(k)}$ before eventually saturating. Note that the interaction includes both energy conserving and non-conserving terms, with the latter giving rise to squeezing of the collective modes. This is closely connected to the macroscopic entanglement properties of the system. Incidentally, two-mode squeezing can be estimated from the reduced covariance matrix $\tilde{V}_{i|j}^{(k)}$ of the system, in terms of its lowest eigenvalue ν^{\min} . The condition $\nu^{\min} < 1/2$ implies that the system is squeezed below the shot noise limit [51, 55], and is thus squeezed. The variation of the lowest ν^{\min} among all stable roots with the effective detuning $\tilde{\Delta}$ of the system is shown in Figs. 3(c)-(d), where it can be directly compared to entanglement.

Further qualitative behavior of entanglement and squeezing in the collective modes can be ascertained by the noise spectrum $S(\omega)$ of the optical mode as shown in Fig. 4. This can be experimentally detected [56] from the light reflected from the cavity as shown in Fig. 1. The calculation of the noise spectrum is shown in Appendix D. The spectrum exhibits level attraction with eigenvalues merging to form exceptional points (EPs) [57, 58] in one of the roots, while level repulsion in another, leading to the formation of entangled hybrid modes of photons and DWs. In Fig. 4(a) for root $k = 1$ we find level attraction in the polaritonic modes formed with a cavity and a collective bright DW mode as they merge just before the resonance $\tilde{\Delta} = -\omega_1$ and separate in the large detuning regime. This leads to two second-order exceptional points. First, at the point where the two modes merge with square root dependency just before resonance $\tilde{\Delta} = -\omega_1$, and the second, where two modes separate again in the large detuning regime. The onset of these two EPs is also associated with the sudden discontinuity in the smallest eigenvalue $\nu_{a|1(2)}^{\min}$ and the associated two-mode squeezing, as shown in Fig. 3(c). There also exists a dark mode at $\omega = \omega_{1(2)}$, seen as a horizontal line at $\omega = \omega_1$ in Figs. 4(a)-(b), which is decoupled from the cavity [59], shows no spectral peaks, and remains invariant with the detuning.

A method to understand the origin of EPs is to consider an effective non-hermitian Hamiltonian. This is obtained by rewriting the linearized QLEs in the form of time-dependent Schrödinger-like equation for the linearized modes $i\partial_t u^{(k)} = \mathcal{H}u^{(k)}$, neglecting the input noise terms. The eigenvalues of \mathcal{H} are directly related to the

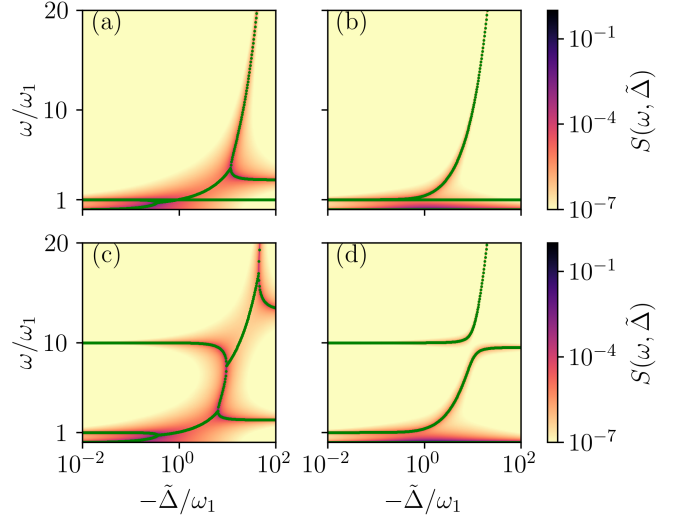


FIG. 4. Output optical spectrum. The plots (a,b) show the spectrum at $\omega_2 = \omega_1$ for the roots $k = 1$ and $k = 2$, which exhibit level attraction and repulsion, respectively. The bottom (c,d) shows the spectrum at $\omega_2 = 10 \omega_1$ for $k = 1$ and $k = 2$, respectively. The green dotted line shows the associated eigenvalues.

drift matrix eigenvalue set as $\{\lambda_H\} = i\{\lambda_A\}$. In particular, for the case of $\kappa_a = \kappa_{1(2)}$, we obtain exact analytical solutions for six eigenvalues of \mathcal{H} . Four of these represent collective bright modes

$$\lambda_{\pm,j}^{(k)} = -i\kappa_a \pm \sqrt{\tilde{\Delta}_{\pm}^{(k)2} + (-1)^j \Theta^2}, \quad (9)$$

where $\Theta^2 = \sqrt{\tilde{\Delta}_{-}^{(k)4} - 8G^2 \bar{n}_a^{(k)} \tilde{\Delta}^{(k)} \omega_1}$ and $\tilde{\Delta}_{\pm}^{(k)2} = (\tilde{\Delta}^{(k)2} \pm \kappa_a^2)/2$. The other two eigenvalues $\lambda_{\pm}^D = -i\kappa_1 \pm \omega_1$ are for non-interacting dark modes. The formation of second-order EPs occur when the term Θ inside the square root in Eq. (9) vanishes, leading to coalescence of eigenvalues and eigenvectors, at $\tilde{\Delta}^{(k)} = -\omega_1 (2Gg_1 \bar{x}_a^{(k)} / \kappa_a)^2$ for $j = 1$ branch. When $\kappa_a \neq \kappa_1$, the eigenvalues need to be numerically obtained from the drift matrix in Eq. (6), however, the dark mode eigenvalues retain the same value λ_{\pm}^D . While crossing these EPs, there are transitions from a region where the real part of two eigenvalues merge while the imaginary part splits as square root and vice versa. Such sudden transition of eigenvalues leads the squeezed state to jump from one stable root to another, leading to a jump in optimal squeezing we see in Fig. 3(c,d).

Similarly, in Fig. 4(b) for $k = 2$, just close to the resonance $\tilde{\Delta} = -\omega_1$, the bright DW mode gets strong level repulsion and the cavity mode remains close to $\omega = 0$ while the dark DW mode again remains invariant for all detunings. Thus, this resonance is associated with the maximum DW-photon entanglement $\mathcal{E}_{a|1(2)}$ as observed in Fig. 3(a). For $\omega_1 \neq \omega_2$, we have two resonances at $\tilde{\Delta} = -\omega_1$ and $-\omega_2 = -10\omega_1$. For root $k = 1$ as shown in Fig. 4(c), these two resonances thus result in two regimes

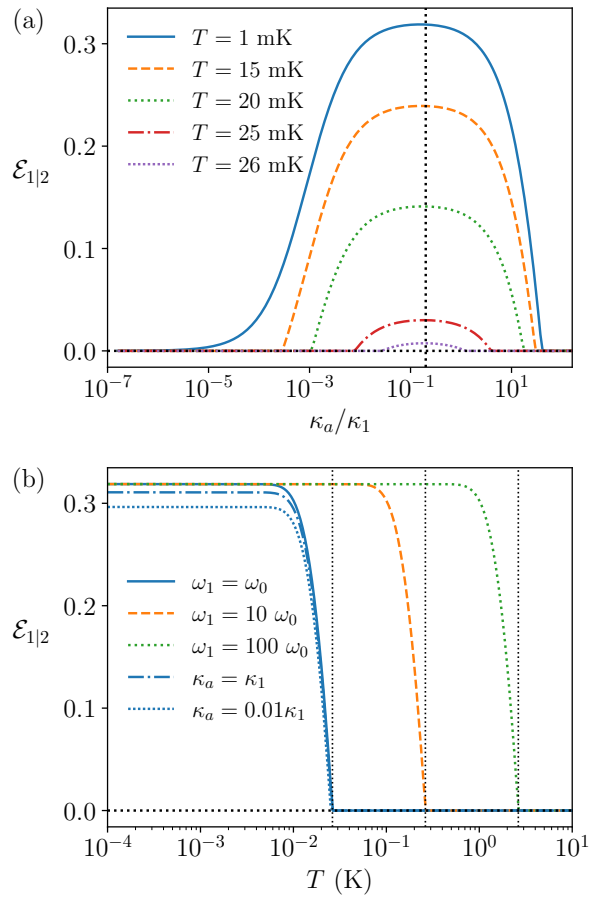


FIG. 5. Thermal stability of macroscopic entanglement between the two domain walls. (a) Plot shows entanglement as a function of the ratio κ_a/κ_1 for different temperatures T . Here $\omega_{1(2)} = \omega_0 = 1$ GHz, $\hat{\Delta} = -40 \omega_{1(2)}$ and $\kappa_1 = 1$ MHz. The vertical black dotted line highlights the maximum entanglement. (b) The plot shows the temperature dependence of $\mathcal{E}_{1|2}$ at fixed $\kappa_a/\kappa_1 = 0.2$ and varying $\omega_{1(2)}/\omega_0 = 1, 10, 100$ with solid blue, orange dashed, and green dotted curves. Now, for fixed $\omega_{1(2)} = \omega_0$, the dissipation is varied, such that $\kappa_a/\kappa_1 = 1$ and 0.01 with blue dot-dashed and dotted curves, respectively. The vertical black dotted lines mark the cutoff temperature $T_c \approx 26$ mK, 0.26 K, and 2.6 K for $\omega_{1(2)} = 1$ GHz, 10 GHz, and 100 GHz, respectively.

of level attraction close to each of these resonances and are thus associated with four second-order EPs, each of which leads to discontinuity in the squeezing $\nu_{a|1}^{\min}$ and $\nu_{a|2}^{\min}$ as shown in Fig. 3(d). Similarly, for root $k = 2$, we see the level repulsion at each of these resonances leading to maximum photon-DW entanglement $\mathcal{E}_{a|1(2)}$ at the respective resonances $\hat{\Delta} = -\omega_{1(2)}$.

An important aspect related to the robustness of the macroscopic entanglement between the two domain walls is thermal stability. In general, thermal fluctuations at finite temperatures are detrimental to entanglement in any dissipative system operating in the GHz regime. In

quantum magnonics, these temperatures are typically in the milli-Kelvin regime [60, 61], which makes it experimentally challenging. Figure 5 shows the variation of entanglement between the two DWs with dissipation and temperature. Within a range of dissipation values, there exists a cutoff temperature T_c beyond which thermal fluctuations prohibit any entanglement between the DWs. First, we note that altering the loss rates of either the photonic (κ_a) or DW modes (κ_1) changes the amount of macroscopic entanglement but not the T_c . Remarkably, reducing κ_a by a factor of 10 has the same positive effect on entanglement as that achieved by increasing κ_1 by a factor of 10. As such the entanglement between the DWs is dependent on the ratio κ_a/κ_1 , as shown in Fig. 5(a), with the maximum achieved at 0.2. However, an improvement of the physically relevant cutoff temperature T_c can be achieved by controlling the pinning potentials. This is due to the fact that number of thermal excitations in DW modes that can negate entanglement, is directly dependent on $\hbar\omega/k_B T$. In fact, an increase of the DW frequency $\omega_{1(2)}$ by an order of magnitude leads directly to an order of magnitude increase in the cut-off temperature T_c . As such, as observed in Fig. 5(b), within realizable experimental parameters, stable, robust entanglement can be sustained between the two domain walls up to 2 K, using DW frequencies of 100 GHz [62, 63].

V. CONCLUSION

The generation of stable and robust entanglement in spin textures and magnons is a challenging task and often requires strong nonlinearity and cryogenic temperatures. In this work, we study the dissipative phases of localized domain walls in a chiral cavity and by controlling the pinning potential and the optical driving, steady-state entanglement is generated between the domain walls. Using states close to the transcritical bifurcation line, entanglement can be switched between photons and DWs to stable entanglement between the two DWs. For suitable, controlled parameters the entanglement can be sustained up to temperatures as high as a few Kelvins. Given recent experimental developments in the study and control of uniaxial magnetic materials, our study provides technologically relevant insight towards entangling stationary spin textures.

Another significant outcome of our study is the optical spectrum for different values of detuning. In the dispersive regime, for the stable roots, there exist both level attraction and repulsion that highlight different regions where strong photon-DW and DW-DW entanglement are generated. The spectrum also shows the emergence of second-order exceptional points in these systems associated with square root spectral splitting, which can be useful for high-precision, magnetic field sensing [64].

Finally, we believe the proposed theoretical scheme can be extended to other chiral spin textures, optomechanical and optomagnonic hybrid systems and prove useful in

various quantum information and computation, quantum communication and quantum sensing applications. An interesting platform is domain walls in ferroelectric systems, where photostrictive effects can give rise to strong interactions [65], and pinned domain walls at THz frequencies can be engineered [66]. This would allow entanglement at temperatures as high as 10 K, which can be relatively easier to setup compared to contemporary cryogenic setups.

ACKNOWLEDGMENTS

We would like to thank K.G. Suresh for valuable discussions. R.G. acknowledges financial support from CSIR-HRDG, India in the form of SRF. H.S.D. acknowledges funding from SERB-DST, India under Core-Research Grant (CRG/2021/008918) and IRCC, IIT Bombay (RD/0521-IRCCSH0-001).

Appendix A: Quantizing and capturing the inverse Faraday effect

As discussed in Sec. II, under strong pinning potential the domain wall (DW) can collectively be treated as a macroscopic particle. In this section, we consider the canonical quantization of a such a DW inside a cavity, interacting through the inverse Faraday effect [38]. In the absence of a cavity field, assuming the presence of a pinning potential $U_{\text{pin}}(X)$, we write down the effective Hamiltonian describing the collective dynamics of a Bloch DW with its center located at position X .

$$\begin{aligned}\mathcal{H}_{\text{DW}} &= \frac{P_X^2}{2m_{\text{eff}}} + U_{\text{pin}}(X) , \\ U_{\text{pin}}(X) &= -K_{\text{pin}} \text{sech}^2 \left(\frac{X}{\lambda_{\text{DW}}} \right)\end{aligned}\quad (\text{A1})$$

where P_X is a canonical momentum obtained from the spin Lagrangian density by shifting to the collective coordinate frame [38], whose details we have omitted here for simplicity. The domain wall width is taken as $\lambda_{\text{DW}} = \sqrt{J/K_{\parallel}}$ where J is the ferromagnetic exchange constant and K_{\parallel} is the in-plane anisotropy field of the material. The pinning potential is typical of the type of a Pöschl-Teller potential, which under a sufficiently strong pinning strength can be approximated under strong pinning strength as a parabolic potential:

$$\begin{aligned}U_{\text{pin}}(X) &= -K_{\text{pin}} \text{sech}^2(X/\lambda_{\text{DW}}) = \frac{-K_{\text{pin}}}{(e^{X/\lambda_{\text{DW}}} + e^{-X/\lambda_{\text{DW}}})^2} \\ &\simeq \frac{-K_{\text{pin}}}{2 + (X/\lambda_{\text{DW}})^2} \simeq K_{\text{pin}} \frac{X^2}{4\lambda_{\text{DW}}^2}\end{aligned}\quad (\text{A2})$$

Thus, under this strong pinning regime, we can quantize the oscillator by defining annihilation operators as $x =$

$x_{\text{zpf}}(b + b^\dagger)$ and $p = -im_{\text{eff}}\omega x_{\text{zpf}}(b - b^\dagger)$, where $x_{\text{zpf}} = \sqrt{\hbar/(2m_{\text{eff}}\omega)}$.

It was realized that when a DW oscillator is placed inside a cavity resonator, it can feel the radiation pressure forces from the electromagnetic field analogous to the optomechanical radiation pressure experienced by a suspended mirror in cavity optomechanics. The origin of such a force here is because of the magneto-optic coupling effect [67] between the electromagnetic field and the spin system. The permittivity tensor gets modulated by the local spin oscillations resulting in the interaction energy

$$\mathcal{H}_{\text{int}} = -\frac{\varepsilon_0}{4} \int \delta\varepsilon_{ij}(\mathbf{S}) \mathcal{E}_i(\mathbf{r}, t) \mathcal{E}_j^*(\mathbf{r}, t) d^3r. \quad (\text{A3})$$

Here, the spin density is given as $\mathbf{S}(\mathbf{r})$, the complex amplitude of the electric field $\mathcal{E}(\mathbf{r}, t)$ is related with original field as $\mathbf{E}(\mathbf{r}, t) = \text{Re}(\mathcal{E}(\mathbf{r}, t)e^{-i\omega_a t})$. The electric field is quantized as $\mathcal{E}(x, t) = -i \sum_{n\lambda} \sqrt{\hbar\omega_n/\epsilon_0 V} \sin(n\pi x/L_{\text{cav}}) \mathbf{e}_\lambda a_{n\lambda}$, here ω_n are the cavity eigenmode frequencies and polarization states in helicity basis are given as $\mathbf{e}_\lambda = (0, \lambda, -i)/\sqrt{2}$, $\lambda \in \{\pm 1\}$. Considering the inverse-Faraday effect induced interaction, the permittivity tensor is given as $\delta\varepsilon_{ij} = if\epsilon_{ijk}S_k$, ϵ_{ijk} is the Levi-Civita symbol, f depends on the Faraday rotation of the sample ϕ_F as $f = 2c\phi_F\sqrt{\varepsilon}/\omega_n$ and S_k is the k^{th} component of spin density $\mathbf{S}(\mathbf{r})$. When N DWs are placed inside the cavity, the cavity frequency depends on the electric permittivity, thus modulating it depending on the position of the DWs, $\mathbf{X}(t) = [X_1(t), X_2(t), \dots, X_N(t)]^T$. Considering the cavity to be centered at eigen frequency $\omega_n = \omega_a(\mathbf{X})$, we obtain the coupling as

$$\begin{aligned}\omega_a(\mathbf{X})a^\dagger a &\simeq \omega_a + \sum_{j=1}^N \frac{\partial\omega_a}{\partial X_j} X_j a^\dagger a, \quad g_j = -\frac{\partial\omega_a(\mathbf{X})}{\partial X_j} x_{\text{zpf}}^j \\ \Rightarrow \mathcal{H}_{\text{int}} &\simeq -\hbar \sum_{j=1}^N g_j (b_j + b_j^\dagger)(a_R^\dagger a_R - a_L^\dagger a_L)\end{aligned}\quad (\text{A4})$$

where a_R , a_L are the cavity annihilation operators for the right- and left-circularly polarized ($\lambda = \pm 1$) states of light. The coupling strength is obtained as $g_j = fS_{\text{eff}}^j\omega_a/4$. The dimensionless geometrical factor $S_{\text{eff}}^j = x_{\text{zpf}}^j A_{\perp}^j/V_c$ depends on the scattering cross-section A_{\perp}^j , the cavity volume V_c and the zero point fluctuation $x_{\text{zpf}}^j = \sqrt{\hbar/2m_j\omega_j}$ of the macroscopic DW, with mass $m_j = \rho V_j$, where ρ is the density of the material and V_j is the effective cross-sectional volume of the DW. We note that higher-order terms and the non-linear Kerr effect have been neglected. Experimentally, it is possible to use a chiral cavity resonator, where one of these polarizations can be fully suppressed [39], allowing us to deal with single-mode interaction $a = a_R$.

Appendix B: Linearizing around steady states

We discuss the linearization of the system around its

steady state, as mentioned in Sec. III. We take the cavity loss rate κ_a and dissipation rate in the domain wall modes as $\kappa_j = \alpha_G \omega_j / \sqrt{K_{\text{pin}}^j l / 2K_{\perp} \lambda_{\text{DW}}}$, where α_G is the Gilbert damping rate [38, 68]. These we use for writing quantum Langevin equations (QLEs) for the Hamiltonian in Eq. (3) are

$$\begin{aligned}\dot{a} &= (i\Delta_a - \kappa_a)a - i \sum_j g_j (b_j + b_j^\dagger)a + \xi + \sqrt{\kappa_a}a^{\text{in}}, \\ \dot{b}_j &= -(i\omega_j + \kappa_j)b_j - ig_j a^\dagger + \sqrt{2\kappa_j}b_j^{\text{in}}.\end{aligned}\quad (\text{B1})$$

These are obtained by writing the Heisenberg equations and adding the input noise operators $a^{\text{in}}, b_j^{\text{in}}$ for the photon and DW modes, respectively. These carry the thermal and quantum noise from the input port and follow the following correlations [40]:

$$\langle a^{\text{in}}(t)a^{\text{in}\dagger}(t') \rangle = (1 + n_a^{\text{th}})\delta(t - t'), \quad (\text{B2})$$

$$\langle a^{\text{in}\dagger}(t)a^{\text{in}}(t') \rangle = n_a^{\text{th}}\delta(t - t'), \quad (\text{B3})$$

$$\langle b_j^{\text{in}}(t)b_j^{\text{in}\dagger}(t') \rangle = (1 + n_j^{\text{th}})\delta(t - t'), \quad (\text{B4})$$

$$\langle b_j^{\text{in}\dagger}(t)b_j^{\text{in}}(t') \rangle = n_j^{\text{th}}\delta(t - t'), \quad (\text{B5})$$

$$n_a^{\text{th}} = (e^{\hbar\omega_a/k_B T} - 1)^{-1}, \quad n_j^{\text{th}} = (e^{\hbar\omega_j/k_B T} - 1)^{-1}. \quad (\text{B6})$$

These noise fluctuations drive the system along with the coherent photon pumping rate ξ . These noise operators have zero mean, $\langle a^{\text{in}} \rangle = \langle b_j^{\text{in}} \rangle = 0$, similarly by defining $\langle a \rangle = \alpha$, $\langle b_j \rangle = \beta_j$, we can write the meanfield representation of Eq. (B1) as

$$\begin{aligned}\dot{\alpha} &= \left[i \left(\Delta_a - \sum_{j=1}^N g_j (\beta_j^* + \beta_j) \right) - \kappa_a \right] \alpha + \xi, \\ \dot{\beta}_j &= -(\kappa_j + i\omega_j)\beta_j - ig_j |\alpha|^2.\end{aligned}\quad (\text{B7})$$

Now, as the system drifts towards the steady state as $t \rightarrow \infty$, we expect these time derivatives to vanish which gives the steady state values as a set of coupled equations. Solving the for steady state gives us the following solution:

$$\bar{\alpha} = \frac{i\xi}{\left(\Delta_a - \sum_{j=1}^N g_j (\bar{\beta}_j^* + \bar{\beta}_j) \right) + i\kappa_a}, \quad (\text{B8})$$

$$\bar{\beta}_j = \frac{-ig_j |\bar{\alpha}|^2}{i\omega_j + \kappa_j}. \quad (\text{B9})$$

These can be further simplified if we substitute $\bar{\alpha} = \sqrt{\bar{n}_\alpha} e^{i\bar{\phi}_\alpha}$, $\bar{\beta}_j = \sqrt{\bar{n}_j} e^{i\bar{\phi}_j}$ and demanding $\bar{n}_\alpha, \bar{n}_j \geq 0$:

$$\bar{n}_\alpha \left[(\Delta_a + \Omega \bar{n}_\alpha)^2 + \kappa_a^2 \right] - \xi^2 = 0, \text{ where} \quad (\text{B10})$$

$$\bar{\phi}_\alpha = \arctan \left(\frac{\kappa_a}{\Delta_a + \Omega \bar{n}_\alpha} \right), \quad \Omega = \sum_{j=1}^N \frac{2g_j^2 \omega_j}{\omega_j^2 + \kappa_j^2}, \quad (\text{B11})$$

$$\bar{n}_j = \frac{g_j^2 \bar{n}_\alpha^2}{\omega_j^2 + \kappa_j^2}, \text{ and } \bar{\phi}_j = \arctan \left(\frac{\kappa_j}{\omega_j} \right). \quad (\text{B12})$$

This will have either one or three solutions for mean photon number, we label them by $\bar{n}_\alpha^{(k)}$, $k \in \{1, 2, 3\}$. Now, we shift the Hamiltonian around these steady state values for each root by transformation $a \rightarrow \alpha + a$, $b_j \rightarrow \beta_j + b_j$ and we rewrite the $H^{(k)}$ in terms of these solutions similar to [51] and obtain:

$$\begin{aligned}H_2^{(k)} &= -\tilde{\Delta}^{(k)} a^\dagger a + \sum_{j=1}^N \omega_j b_j^\dagger b_j, \\ &+ \sum_{j=1}^N g_j \left(\alpha^{(k)} a^\dagger + \alpha^{*(k)} a \right) (b_j + b_j^\dagger), \\ H^{(k)} &= H_2^{(k)} + H_3.\end{aligned}\quad (\text{B13})$$

Now at this stage, a simplification is possible if we make $|\alpha| \gg 1$, which enables us to drop the cubic term in fluctuations, leading to a simplified quadratic Hamiltonian which leads to Gaussian dynamics. We have ensured that this condition is maintained for all our results.

Appendix C: Adiabatic Elimination

The linearized Langevin equations can be written as

$$\begin{aligned}\delta\dot{a} &= (i\tilde{\Delta} - \kappa_a)\delta a - i\alpha \sum_{j=1}^N g_j (\delta b_j^\dagger + \delta b_j) + \sqrt{2\kappa_a}a^{\text{in}}, \\ \delta\dot{b}_j &= -(\kappa_j + i\omega_j)\delta b_j - ig_j (\alpha^* \delta a + \alpha \delta a^\dagger) + \sqrt{2\kappa_j}b_j^{\text{in}}.\end{aligned}\quad (\text{C1})$$

Now, since we are interested in large detuning regime ($\omega_j, \tilde{\Delta} \gg \alpha g_j, \forall j$), we define slowly evolving variables $\delta\tilde{a} = e^{(-i\tilde{\Delta} + \kappa_a)t} \delta a$, $\tilde{b}_j = e^{(i\omega_j^{\text{eff}} + \kappa_j)t} b_j$, where we have shifted the mechanical frequency and damping to accommodate for the collective optical spring effect. The cavity part in this frame is obtained as

$$\begin{aligned}\delta\dot{\tilde{a}} &= -i\alpha \sum_{j=1}^N g_j \left[\delta\tilde{b}_j^\dagger e^{i(\omega_j^{\text{eff}} - \tilde{\Delta})t + (\kappa_a - \kappa_j^{\text{eff}})t} \right. \\ &\left. + \delta\tilde{b}_j e^{-i(\omega_j^{\text{eff}} + \tilde{\Delta})t + (\kappa_a - \kappa_j^{\text{eff}})t} \right] + \sqrt{2\kappa_a}\tilde{a}^{\text{in}}.\end{aligned}\quad (\text{C2})$$

We solve the above equation by taking the slowly varying operators outside of the integration over time from $-\infty$ to zero assuming ($\kappa_a \geq \kappa_j$) to obtain

$$\begin{aligned}\delta\tilde{a} &= -i\alpha \sum_{j=1}^N g_j \left[\frac{\delta\tilde{b}_j^\dagger e^{i(\omega_j^{\text{eff}} - \tilde{\Delta})t + (\kappa_a - \kappa_j^{\text{eff}})t}}{i(\omega_j^{\text{eff}} - \tilde{\Delta}) + \kappa_a - \kappa_j^{\text{eff}}} \right. \\ &\left. + \frac{\delta\tilde{b}_j e^{-i(\omega_j^{\text{eff}} + \tilde{\Delta})t + (\kappa_a - \kappa_j^{\text{eff}})t}}{-i(\omega_j^{\text{eff}} + \tilde{\Delta}) + \kappa_a - \kappa_j^{\text{eff}}} \right], \text{ where}\end{aligned}\quad (\text{C3})$$

$$\begin{aligned}\delta a &= -i\alpha \sum_{j=1}^N g_j \left[\frac{\delta b_j^\dagger}{i(\omega_j^{\text{eff}} - \tilde{\Delta}) + \kappa_a - \kappa_j^{\text{eff}}} \right. \\ &\left. + \frac{\delta b_j}{-i(\omega_j^{\text{eff}} + \tilde{\Delta}) + \kappa_a - \kappa_j^{\text{eff}}} \right],\end{aligned}\quad (\text{C4})$$

$$\delta a = \sum_{j=1}^N \left(G_j^- \delta b_j^\dagger + G_j^+ \delta b_j \right). \quad (\text{C5})$$

Substituting this back to the linear equation Eq. (C1):

$$\begin{aligned} \delta \dot{b}_j &= -(\kappa_j + i\omega_j) \delta b_j - \sum_{k=1}^N i \left(G_{j,k} \delta b_k^\dagger - G_{j,k}^* \delta b_k \right), \\ G_{jk} &= \frac{2\tilde{\Delta} |\alpha|^2 g_j g_k}{(i\omega_k^{\text{eff}} + \Delta \kappa_k)^2 + \tilde{\Delta}^2}, \quad \Delta \kappa_k = \kappa_a - \kappa_k^{\text{eff}}. \quad (\text{C6}) \\ \delta \dot{b}_j &= -(\kappa_j^{\text{eff}} + i\omega_j^{\text{eff}}) \delta b_j - i G_{jj} b_j^\dagger \\ &\quad - \sum_{k \neq j} i \left(G_{j,k} \delta b_k^\dagger - G_{j,k}^* \delta b_k \right), \\ \omega_j^{\text{eff}} &= \omega_j - \text{Re}(G_{jj}^*), \quad \kappa_j^{\text{eff}} = \kappa_j + \text{Im}(G_{jj}^*). \quad (\text{C7}) \end{aligned}$$

By solving the Eq. (C7), one can obtain the shifted damping and frequency induced by the collective optical spring effect. The quadratic interaction Hamiltonian H_{eff} after adiabatic elimination is

$$\begin{aligned} H_{\text{int}}^{\text{ad}} &= \sum_{j,k} \left(G_{j,k} \delta b_j \delta b_k^\dagger + G_{j,k}^* \delta b_j^\dagger \delta b_k \right) \\ &\quad + \sum_{j,k} \left(G_{j,k} \delta b_j^\dagger \delta b_k^\dagger + G_{j,k}^* \delta b_j \delta b_k \right), \quad (\text{C8}) \end{aligned}$$

while the non-interacting Hamiltonian is given by

$$\begin{aligned} H_0^{\text{ad}} &= -\tilde{\Delta} \sum_{j,k} \left(G_j^{+*} G_k^+ \delta b_j^\dagger b_k + G_j^{-*} G_k^- \delta b_j b_k^\dagger \right) \\ &\quad - \tilde{\Delta} \sum_{j,k} \left(G_j^{+*} G_k^- \delta b_j^\dagger b_k^\dagger + G_j^{-*} G_k^+ \delta b_j b_k \right) \\ &\quad + \sum_j \omega_j \delta b_j^\dagger \delta b_j. \quad (\text{C9}) \end{aligned}$$

Collecting and identifying relevant quadratic terms in the full adiabatic Hamiltonian $H^{\text{ad}} = H_0^{\text{ad}} + H_{\text{int}}^{\text{ad}}$, we get:

$$\begin{aligned} H^{\text{ad}} &= \sum_j \left[\omega_j^{\text{eff}} \delta b_j^\dagger b_j + \frac{1}{2} \left(G_{jj} \delta b_j^{\dagger 2} + G_{jj}^* \delta b_j^2 \right) \right] \\ &\quad + \sum_{j,k}^{j \neq k} \left(\nu_{j,k}^+ \delta b_j^\dagger \delta b_k + \nu_{j,k}^- \delta b_j \delta b_k^\dagger \right) \\ &\quad + \sum_{j,k}^{j \neq k} \left(\mu_{j,k} \delta b_j^\dagger \delta b_k^\dagger + \mu_{j,k}^* \delta b_j b_k \right), \quad \text{where} \quad (\text{C10}) \\ \omega_j^{\text{eff}} &= \omega_j + 2\text{Re}(G_{jj}) - \tilde{\Delta} (|G_j^+|^2 + |G_j^-|^2), \\ \nu_{j,k}^- &= G_{j,k} - \tilde{\Delta} G_j^{-*} G_k^-, \quad \nu_{j,k}^+ = G_{j,k}^* - \tilde{\Delta} G_j^{+*} G_k^+, \quad \text{and} \\ \mu_{j,k} &= G_{j,k} - \tilde{\Delta} G_j^{+*} G_k^-. \quad (\text{C11}) \end{aligned}$$

Using this total adiabatic Hamiltonian, we obtain the Langevin equations of motion:

$$\begin{aligned} i\delta \dot{b}_j &= (\omega_j^{\text{eff}} - i\kappa_j) \delta b_j + G_{jj} \delta b_j^\dagger + \sum_{k \neq j} \left(\nu_{j,k}^+ \delta b_k + \mu_{j,k} \delta b_k^\dagger \right), \\ i\delta \dot{b}_j^\dagger &= (-\omega_j^{\text{eff}} - i\kappa_j) \delta b_j^\dagger - G_{jj}^* \delta b_j - \sum_{k \neq j} \left(\nu_{j,k}^- \delta b_k^\dagger + \mu_{j,k}^* \delta b_k \right). \quad (\text{C12}) \end{aligned}$$

We note that this gives different strengths for beam splitter interaction and for two mode squeezing interaction, which is different from what one obtains from very large detuning regime ($\tilde{\Delta} \gg \omega_j \geq |\alpha g_j|$). For such a regime a great simplification is possible using

$$G_{j,k}^{\text{eff}} \simeq \frac{2|\alpha|^2 g_j g_k}{\tilde{\Delta}}, \quad G_j^\pm \simeq \frac{\alpha g_j}{\tilde{\Delta}}, \quad \nu_{j,k} = \mu_{j,k} \simeq \frac{|\alpha|^2 g_j g_k}{\tilde{\Delta}}.$$

This is what one can also obtain from the second-order perturbation theory assuming that cavity fluctuations remain in a vacuum state in the zeroth order [69], however, this leads to symmetric coefficients. Our results are valid even in a regime where resonances are dominant and where these coefficients are quite different, and they extend to the large detuning regime.

Appendix D: Output Optical Spectrum

In this section, we connect the dissipative phases associated with DW-DW entanglement to the experimentally observable optical spectrum [56]. This is measured by collecting the reflected output light and passing it through a spectrum analyzer as shown in Fig. 1.

For this, here we provide a simple compact matrix method to calculate the spectrum for any quadrature set. The linearized quantum Langevin equations can be written in matrix form and expressed in the frequency domain:

$$\begin{aligned} \dot{u} &= Au + D_0 u^{\text{in}}, \quad \text{where } \eta = D_0 u^{\text{in}}, \\ u(\omega) &= -(A + i\omega I)^{-1} D_0 u^{\text{in}}(\omega). \quad (\text{D1}) \end{aligned}$$

Then we combine it with input-output formalism to write the output operators in terms of the input noise operators

$$\begin{aligned} u^{\text{out}}(\omega) &= D_0 u(\omega) - u^{\text{in}}(\omega), \\ u^{\text{out}}(\omega) &= -[I + D_0(A + i\omega I)^{-1} D_0] u^{\text{in}}(\omega) = \mathcal{T}(\omega) u^{\text{in}}(\omega). \quad (\text{D2}) \end{aligned}$$

The output spectral function $S_{i,j}(\omega)$ for correlations between $u_i^{\text{out}}, u_j^{\text{out}}$ quadrature operators can be written as

$$\begin{aligned} S_{i,j}(\omega) &= \frac{1}{2\pi} \int_{-\infty}^{\infty} \langle u_i^{\text{out}}(\omega) u_j^{\text{out}}(\omega') \rangle d\omega', \\ S_{i,j}(\omega) &= \frac{1}{2\pi} \sum_{k,l} \int_{-\infty}^{\infty} \mathcal{T}_{i,k}(\omega) \mathcal{T}_{j,l}(\omega') \langle u_k^{\text{in}}(\omega) u_l^{\text{in}}(\omega') \rangle d\omega'. \quad (\text{D3}) \end{aligned}$$

All the expectation values can be combined in the form of a matrix χ : $\langle u_k^{\text{in}}(\omega) u_l^{\text{in}}(\omega') \rangle = 2\pi \chi_{k,l}(\omega) \delta(\omega + \omega')$. The expression of spectral function then simplifies to

$$\begin{aligned} S_{i,j}(\omega) &= \sum_{k,l} \int_{-\infty}^{\infty} \mathcal{T}_{i,k}(\omega) \mathcal{T}_{j,l}(\omega') \chi_{k,l}(\omega) \delta(\omega + \omega') d\omega', \\ S_{i,j}(\omega) &= \sum_{k,l} \mathcal{T}_{i,k}(\omega) \chi_{k,l}(\omega) \mathcal{T}_{j,l}(-\omega), \text{ and} \\ \mathcal{S}(\omega) &= \mathcal{T}(\omega) \chi(\omega) \mathcal{T}^T(-\omega). \end{aligned} \quad (\text{D4})$$

The optical output spectrum is then obtained by summing over both the position and momentum cavity quadrature correlations $S(\omega) = S_{x_a, x_a}(\omega) + S_{p_a, p_a}(\omega)$.

-
- [1] Y. M. Bunkov, *Journal of Experimental and Theoretical Physics* **131**, 18 (2020).
 - [2] H. Yuan, Y. Cao, A. Kamra, R. A. Duine, and P. Yan, *Physics Reports* **965**, 1 (2022).
 - [3] D. Lachance-Quirion, Y. Tabuchi, A. Gloppe, K. Usami, and Y. Nakamura, *Applied Physics Express* **12**, 070101 (2019).
 - [4] D. D. Awschalom, C. R. Du, R. He, F. J. Heremans, A. Hoffmann, J. Hou, H. Kurebayashi, Y. Li, L. Liu, V. Novosad, J. Sklenar, S. E. Sullivan, D. Sun, H. Tang, V. Tyberkevych, C. Trevillian, A. W. Tsen, L. R. Weiss, W. Zhang, X. Zhang, L. Zhao, and C. W. Zollitsch, *IEEE Transactions on Quantum Engineering* **2**, 1 (2021).
 - [5] X. Zhang, *Materials Today Electronics* **5**, 100044 (2023).
 - [6] B. Flebus, S. M. Rezende, D. Grundler, and A. Barman, *Journal of Applied Physics* **133**, 160401 (2023).
 - [7] S. N. Andrianov and S. A. Moiseev, *Phys. Rev. A* **90**, 042303 (2014).
 - [8] J. Simon, H. Tanji, S. Ghosh, and V. Vuletić, *Nature Physics* **3**, 765 (2007).
 - [9] X.-F. Pan, P.-B. Li, X.-L. Hei, X. Zhang, M. Mochizuki, F.-L. Li, and F. Nori, *Phys. Rev. Lett.* **132**, 193601 (2024).
 - [10] A. V. Chumak, V. I. Vasyuchka, A. A. Serga, and B. Hillebrands, *Nature Physics* **11**, 453 (2015).
 - [11] S. Emori, U. Bauer, S.-M. Ahn, E. Martinez, and G. S. D. Beach, *Nature Materials* **12**, 611 (2013).
 - [12] X. Li, C. Collignon, L. Xu, H. Zuo, A. Cavanna, U. Gennser, D. Mailly, B. Fauqué, L. Balents, Z. Zhu, and K. Behnia, *Nat. Commun.* **10**, 3021 (2019).
 - [13] G. Finocchio, F. Büttner, R. Tomasello, M. Carpentieri, and M. Kläui, *Journal of Physics D: Applied Physics* **49**, 423001 (2016).
 - [14] A. Bogdanov and A. Hubert, *Journal of Magnetism and Magnetic Materials* **138**, 255 (1994).
 - [15] J.-P. Krumme, I. Bartels, B. Strocka, K. Witter, C. Schmelzer, and R. Spohr, *J. Appl. Phys.* **48**, 5191 (1977).
 - [16] C. Hanneken, A. Kubetzka, K. von Bergmann, and R. Wiesendanger, *New J. Phys.* **18**, 055009 (2016).
 - [17] C. Holl, M. Knol, M. Pratzer, J. Chico, I. L. Fernandes, S. Lounis, and M. Morgenstern, *Nat. Commun.* **11**, 2833 (2020).
 - [18] A. Haller, S. Groenendijk, A. Habibi, A. Michels, and T. L. Schmidt, *Phys. Rev. Res.* **4**, 043113 (2022).
 - [19] A. Finco, A. Haykal, R. Tanos, F. Fabre, S. Chouaieb, W. Akhtar, I. Robert-Philip, W. Legrand, F. Ajejas, K. Bouzehouane, N. Reyren, T. Devolder, J.-P. Adam, J.-V. Kim, V. Cros, and V. Jacques, *Nat. Commun.* **12**, 767 (2021).
 - [20] X. Yu, *Journal of Magnetism and Magnetic Materials* **539**, 168332 (2021).
 - [21] S. Parkin and S.-H. Yang, *Nat. Nanotechnol.* **10**, 195 (2015).
 - [22] N. Nagaosa and Y. Tokura, *Nat. Nanotechnol.* **8**, 899 (2013).
 - [23] Y. Zhou, S. Li, X. Liang, and Y. Zhou, *Advanced Materials* **37**, 2312935 (2025).
 - [24] R. V. Ababei, M. O. A. Ellis, I. T. Vidamour, D. S. Devadasan, D. A. Allwood, E. Vasilaki, and T. J. Hayward, *Sci. Rep.* **11**, 15587 (2021).
 - [25] O. Lee, R. Msiska, M. A. Brems, M. Kläui, H. Kurebayashi, and K. Everschor-Sitte, *Applied Physics Letters* **122**, 260501 (2023).
 - [26] G. Park and S.-K. Kim, *Phys. Rev. B* **109**, 174420 (2024).
 - [27] J. Zou, S. Bosco, B. Pal, S. S. P. Parkin, J. Klinovaja, and D. Loss, *Phys. Rev. Res.* **5**, 033166 (2023).
 - [28] C. Psaroudaki, E. Peraticos, and C. Panagopoulos, *Applied Physics Letters* **123**, 260501 (2023).
 - [29] J. Li and S.-Y. Zhu, *New Journal of Physics* **21**, 085001 (2019).
 - [30] Z. Zhang, M. O. Scully, and G. S. Agarwal, *Phys. Rev. Res.* **1**, 023021 (2019).
 - [31] D.-W. Luo, X.-F. Qian, and T. Yu, *Optics Letters* **46**, 1073 (2021).
 - [32] M. Yu, S.-Y. Zhu, and J. Li, *Journal of Physics B: Atomic, Molecular and Optical Physics* **53**, 065402 (2020).
 - [33] H. Y. Yuan, S. Zheng, Z. Ficek, Q. Y. He, and M.-H. Yung, *Phys. Rev. B* **101**, 014419 (2020).
 - [34] Y. Liu, A. Bergman, A. Bagrov, A. Delin, D. Thonig, M. Pereiro, O. Eriksson, S. Streib, E. Sjöqvist, and V. Azimi-Mousolou, *New Journal of Physics* **25**, 113032 (2023).
 - [35] S. K. Karna, M. Marshall, W. Xie, L. DeBeer-Schmitt, D. P. Young, I. Vekhter, W. A. Shelton, A. Kovács, M. Charilaou, and J. F. DiTusa, *Nano Lett.* **21**, 1205 (2021).
 - [36] G. Catalan, J. Seidel, R. Ramesh, and J. F. Scott, *Rev. Mod. Phys.* **84**, 119 (2012).
 - [37] S.-H. Yang, R. Naaman, Y. Paltiel, and S. S. P. Parkin, *Nat. Rev. Phys.* **3**, 328 (2021).
 - [38] I. Proskurin, A. S. Ovchinnikov, J.-i. Kishine, and R. L. Stamps, *Phys. Rev. B* **98**, 220411 (2018).
 - [39] K. Voronin, A. S. Taradin, M. V. Gorkunov, and D. G. Baranov, *ACS Photonics* **9**, 2652 (2022).

- [40] M. Aspelmeier, T. J. Kippenberg, and F. Marquardt, *Rev. Mod. Phys.* **86**, 1391 (2014).
- [41] R. C. Sherwood, J. P. Remeika, and H. J. Williams, *Journal of Applied Physics* **30**, 217 (1959).
- [42] A. H. Bobeck, *Bell System Technical Journal* **46**, 1901 (1967).
- [43] A. Malozemoff and J. Slonczewski, *Magnetic Domain Walls in Bubble Materials*, Applied solid state science (Academic Press, 1979).
- [44] A. Thiaville and J. Miltat, Topology and magnetic domain walls, in *Topology in Magnetism* (Springer International Publishing, 2018) pp. 41–73.
- [45] R. Schafer, W. Ho, J. Yamasaki, A. Hubert, and F. Humphrey, *IEEE Transactions on Magnetics* **27**, 3678 (1991).
- [46] A. B. Kashuba and V. L. Pokrovsky, *Physical Review B* **48**, 10335 (1993).
- [47] T. Jourdan, F. Lançon, and A. Marty, *Phys. Rev. B* **75**, 094422 (2007).
- [48] T. Koyama, D. Chiba, K. Ueda, K. Kondou, H. Tanigawa, S. Fukami, T. Suzuki, N. Ohshima, N. Ishiwata, Y. Nakatani, K. Kobayashi, and T. Ono, *Nature Materials* **10**, 194 (2011).
- [49] H. Hübener, U. De Giovannini, C. Schäfer, J. Andberger, M. Ruggenthaler, J. Faist, and A. Rubio, *Nature Materials* **20**, 438 (2020).
- [50] R. R. Riso, L. Grazioli, E. Ronca, T. Giovannini, and H. Koch, *Phys. Rev. X* **13**, 031002 (2023).
- [51] F. Bibak, U. DeliĆ, M. Aspelmeier, and B. Dakić, *Phys. Rev. A* **107**, 053505 (2023).
- [52] R. Simon, *Physical Review Letters* **84**, 2726 (2000).
- [53] B. M. Terhal, *IBM Journal of Research and Development* **48**, 71 (2004).
- [54] T. Hiroshima, G. Adesso, and F. Illuminati, *Phys. Rev. Lett.* **98**, 050503 (2007).
- [55] R. Simon, N. Mukunda, and B. Dutta, *Phys. Rev. A* **49**, 1567 (1994).
- [56] Y. Li, V. G. Yefremenko, M. Lisovenko, C. Trevillian, T. Polakovic, T. W. Cecil, P. S. Barry, J. Pearson, R. Divan, V. Tyberkevych, C. L. Chang, U. Welp, W.-K. Kwok, and V. Novosad, *Phys. Rev. Lett.* **128**, 047701 (2022).
- [57] C. Dembowski, H.-D. Gräf, H. L. Harney, A. Heine, W. D. Heiss, H. Rehfeld, and A. Richter, *Physical Review Letters* **86**, 787 (2001).
- [58] W. D. Heiss, *Journal of Physics A: Mathematical and General* **37**, 2455 (2004).
- [59] M. C. Kuzyk and H. Wang, *Phys. Rev. A* **96**, 023860 (2017).
- [60] Y. Tabuchi, S. Ishino, A. Noguchi, T. Ishikawa, R. Yamazaki, K. Usami, and Y. Nakamura, *Science* **349**, 405 (2015).
- [61] S. Bayati, A. Mahdifar, and M. Bagheri Harouni, *Phys. Rev. A* **110**, 013710 (2024).
- [62] M. Voto, L. Lopez-Diaz, and E. Martinez, *Sci. Rep.* **7** (2017).
- [63] T. Herranen and L. Laurson, *Phys. Rev. B* **96**, 144422 (2017).
- [64] X.-g. Wang, G.-h. Guo, and J. Berakdar, *Phys. Rev. Appl.* **15**, 034050 (2021).
- [65] F. Rubio-Marcos, A. Del Campo, P. Marchet, and J. F. Fernández, *Nature Communications* **6**, 6594 (2015).
- [66] J. Hlinka, M. Paściak, S. Körbel, and P. Marton, *Phys. Rev. Lett.* **119**, 057604 (2017).
- [67] M. G. Cottam and D. J. Lockwood, *Light scattering in magnetic solids*, xiv, 248 p. (Wiley, New York, 1986) pp. xiv, 248 p.
- [68] G. Tatara, H. Kohno, and J. Shibata, *Physics Reports* **468**, 213 (2008).
- [69] M. Schmidt, M. Ludwig, and F. Marquardt, *New Journal of Physics* **14**, 125005 (2012).